Coiled Coils at the Edge of Configurational Heterogeneity. Structural Analyses of Parallel and Antiparallel Homotetrameric Coiled Coils Reveal Configurational Sensitivity to a Single Solvent-Exposed Amino Acid Substitution[†,‡]

Maneesh K. Yadav,[§] Luke J. Leman,[§] Daniel J. Price, Charles L. Brooks III, C. David Stout, and M. Reza Ghadiri*

Departments of Chemistry and Molecular Biology, and The Skaggs Institute of Chemical Biology, The Scripps Research Institute, 10550 North Torrey Pines Road, La Jolla, California 92037

Received January 16, 2006; Revised Manuscript Received February 15, 2006

ABSTRACT: A detailed understanding of the mechanisms by which particular amino acid sequences can give rise to more than one folded structure, such as for proteins that undergo large conformational changes or misfolding, is a long-standing objective of protein chemistry. Here, we describe the crystal structures of a single coiled-coil peptide in distinct parallel and antiparallel tetrameric configurations and further describe the parallel or antiparallel crystal structures of several related peptide sequences; the antiparallel tetrameric assemblies represent the first crystal structures of GCN4-derived peptides exhibiting such a configuration. Intriguingly, substitution of a single solvent-exposed residue enabled the parallel coiled-coil tetramer GCN4-pLI to populate the antiparallel configuration, suggesting that the two configurations are close enough in energy for subtle sequence changes to have important structural consequences. We present a structural analysis of the small changes to the helix register and side-chain conformations that accommodate the two configurations and have supplemented these results using solution studies and a molecular dynamics energetic analysis using a replica exchange methodology. Considering the previous examples of structural nonspecificity in coiled-coil peptides, the findings reported here not only emphasize the predisposition of the coiled-coil motif to adopt multiple configurations but also call attention to the associated risk that observed crytstal structures may not represent the only (or even the major) species present in solution.

The diverse functional prowess of proteins derives in large part from their ability to adopt unique tertiary and quaternary structures, and a major goal of protein chemistry is thus to understand in detail how primary amino acid sequences specify three-dimensional structures. Conformational changes and protein misfolding are critical events in biological processes and diseases in which a given polypeptide sequence gives rise to more than one folded structure, but detailed structural analyses of such processes are often difficult because multiple conformations usually result in intractably complex nuclear magnetic resonance (NMR) spectra and/or interfere with crystallization. We believe that the structural characterization and analysis of naturally derived peptides can provide simplified models for understanding folding and structure in proteins, especially for technically demanding problems such as the basis of conformational specificity.

The coiled coil (*1*) is a widespread motif in biology and has proven to be not only a valuable model for investigating protein folding and stability but also an attractive scaffold for protein engineering. Folding of the coiled-coil motif is driven primarily by the burial of a hydrophobic core between two or more supercoiled α helices. The best-studied family of coiled coils is that derived from the leucine zipper of the yeast transcription factor GCN4 (*2*), for which many peptide derivatives have been structurally characterized (*3−17*). Notably, several GCN4-derived peptides have been reported to populate more than one configuration. In one instance, a single sequence was crystallized in both the dimeric and trimeric configurations, allowing for a detailed analysis of the determinants of the oligomerization state (*7*). For another sequence that forms predominantly coiled-coil dimers (in the absence of benzene) or trimers (in the presence of benzene) in solution (*8*), crystal structures have been reported for both the parallel (*8*) and antiparallel (*15*) trimeric configurations. Further, substituting a triazole into the backbone of a tetrameric GCN4-derived peptide caused the sequence to exist mainly as dimers in solution, but the tetrameric state was observed in the crystal structure (*16*). Not surprisingly, nearly all previously reported changes to the coiled-coil configuration have been induced by substitutions of residues in the hydrophobic core.

To date, the most widely studied coiled coils are peptide sequences that form parallel helical assemblies, in which individual helices in the bundle are aligned in the same N → C direction (*3−14*, *18*, *19*). In contrast, the antiparallel coiled coils, for which rational design principles have only

recently been specified (*20*−*26*), are less structurally scrutinized (*15*, *27*−*30*). Both configurations play critical roles in biology, acting for example as oligomerization domains, sites of protein/protein recognition, and nucleic-acid-binding elements (*31*−*33*). Further, switching between parallel and antiparallel conformations has recently been implicated in a regulatory role for natural coiled coils (*34*). Unraveling the underlying principles of parallel/antiparallel coiled-coil formation would thus facilitate our understanding of these biological processes; additionally, control over the helical configuration would provide protein designers an enriched ability to create diverse functional assemblies.

Here, we describe the crystal structures of a single coiled-coil peptide in distinct parallel and antiparallel tetrameric configurations and further describe the parallel or antiparallel crystal structures of several related peptide sequences. The antiparallel tetrameric assemblies reported here represent the first crystal structures of GCN4-derived peptides exhibiting such a configuration, and it is noteworthy that substitution of a single solvent-exposed glutamic acid residue in the 33-residue GCN4-pLI (*4*) enabled the switch in the crystallographic structure from the commonly observed parallel coiled coil to the antiparallel arrangement. We have supplemented these findings using an equilibrium disulfide-exchange experiment and an analysis from atomistic simulations utilizing the well-documented replica exchange (REX)[1] methodology (*35*) (to permit a "competition" of parallel and antiparallel structures) to better understand the energetic differences between the configurations in solution. The crystal structures of a single peptide sequence in two distinct supramolecular forms provide a rare glimpse into the malleability of interhelical packing interactions, offer valuable models for the structure-based design of helical proteins and biomaterials, and call attention to the small energetic differences between discrete coiled-coil assemblies that can engender striking structural consequences upon subtle amino acid substitutions.

MATERIALS AND METHODS

Materials. Fmoc-Arg(Pbf)-Wang resin, *N*-hydroxybenzotriazole (HOBt), and all protected amino acids were obtained from Novabiochem. Solvents and all other chemicals were obtained from Aldrich or Fisher and used without further purification.

Peptide Synthesis. Peptides were prepared using Fmoc-Arg(Pbf)-Wang resin using an Advanced ChemTech 348Ω automated synthesizer, with diisopropylcarbodiimide (DIC)/HOBt in *N*-methylpyrrolidinone (NMP) for couplings and 30% piperidine in NMP for removal of the Fmoc-protecting group. Acetylation was performed with 50% acetic anhydride in NMP. Side-chain-protecting groups were Cys(Trt), Arg-(Pbf), Ser(tBu), Lys(Boc), Glu(tBu), Asp(tBu), Tyr(tBu), Gln(Trt), Asn(Trt), and His(Trt). Cleavage of peptides was typically effected with a mixture of 94:2.5:2.5:1 trifluoro-

acetic acid (TFA)/ethanedithiol/water/triisopropylsilane for 4 h. Peptides were precipitated with ether (50 mL), centrifuged, and washed with ether. After drying in vacuo, peptides were purified on a C18 column (Vydac 218TP) eluting with a water/acetonitrile/TFA gradient and lyophilized. Molecular weights and purities of peptides were verified using a PerSeptive Biosystems Voyager DE NOVO matrix-assisted laser desorption ionization time-of-flight (MALDI−TOF) mass spectrometer and analytical high-performance liquid chromatography (HPLC). The *S*-acetamide adduct of peptide **3** was synthesized by reacting purified peptide (8 mg) with iodoacetamide (40 equiv) for 45 min, with the resulting product being confirmed by MALDI−TOF and repurified by HPLC.

Crystallization. Hampton I, II, Cryo (Hampton Research Co.) and Wizard I, II (Emerald Biosystems) crystallization screens were initially applied in hanging drop vapor diffusion experiments to determine crystallization conditions for peptide **2**, using 10 mg/mL stocks of peptide in water. Initial screens consisted of 1 μL of peptide stock and 1 μL of buffer over a well containing 0.5 mL of buffer. The buffers yielding crystals are listed below. Crystal growth was refined by applying different ratios of peptide stock to reservoir buffer, and in general, better crystals resulted from applying larger volumes of peptide stock (1−2 μL) to smaller volumes of reservoir buffer (0.2−1 μL). The reported crystals do not grow exclusively under the conditions that we report here; a number of other screened reservoir solutions (with different pH values) yielded crystals with the same morphologies and lattice parameters.

For all peptides crystallized in the parallel configuration, the buffer used was 10% PEG 6000 and 2.0 M NaCl (Hampton Crystal Screen 2, #1). For all peptides crystallized in the antiparallel configuration, the buffer used was 30% PEG 400 and 100 mM 3-cyclohexylamino-1-propane-sulfonic acid (CAPS) at pH 10.5 (Wizard 1 #5), with the exceptions of peptide **6**, which crystallized from 70 mM trisodium citrate dihydrate at pH 5.6, 0.7 M ammonium dihydrogen phosphate, and 30% glycerol (Hampton Cryo #11), and peptide **10**, which crystallized from a solution of 20% PEG 3350 in 200 mM KSCN. Although the pH of the CAPS buffer is relatively high, residual TFA in the peptide stock solutions caused the actual pH in crystallization drops to be much lower (pH < 5). Only E20S (peptide **4**) was observed to crystallize in both the parallel and antiparallel configurations (under the respective buffer conditions described above). The tetragonal crystal form tended to grow epitaxially twinned, but we were fortunate to obtain a single crystal of E20C (peptide **3**) by splitting it down the cleavage plane with a loop.

Crystal Structure Determination and Refinement. See Table S1 in the Supporting Information for all crystallization statistics. Integration and scaling for all datasets was carried out with CrystalClear (MSC) (*36*) and the CCP4 suite of programs (*37*, *38*). Our initial antiparallel structure determination was carried out on peptide **2**. We used MALDI−TOF to identify heavy metals that formed peptide adducts by co-spotting microliter volumes of ∼2 mM peptide crystallization stock and ∼50 mM heavy-metal solution in water. Potassium dicyanoaurate (I) was found to give a clean adduct. A heavy atom derivative of peptide **2**[Se] (containing a selenomethionine residue instead of methionine at position

---

[1] Abbreviations: ABA, acetamidobenzoic acid; CD, circular dichroism; Cys, cysteine, Glu, glutamic acid; HPLC, high-performance liquid chromatography; Lys, lysine; MALDI−TOF, matrix-assisted laser desorption ionization time-of-flight; MW, molecular weight; N_{agg}, apparent aggregation number; REX, replica exchange; rmsd, root-mean-square deviation; Ser, serine; SEC, size-exclusion chromatography; T_m, melting temperature; UV, ultraviolet.

2) was prepared by growing crystals in their native condition and then adding a small volume (0.5 μL) of 50 mM potassium dicyanoaurate (I) in water to the drop containing crystals. The soaked crystal was harvested after 24 h and mounted for data collection using an MSC R-Axis IV (Cu Kα, λ = 1.54 Å). Upon completion of a $\sim$13-fold redundant dataset, sharp peaks were seen in the anomalous difference Patterson map [Au(f',f'') = (−4.3,7.3) for Cu Kα]. SOLVE/RESOLVE (*39*−*41*) was employed for single isomorphous replacement with anomalous signal (SIRAS) phasing between the datasets from underivatized 2^{Se} and the heavy-atom-soaked derivative. Six gold sites were identified near the Cys20/His17 regions and were used to generate a model that was approximately 50% complete. This model and the dataset for underivatized peptide **2** were directly fed to ARP/wARP (*42*), which provided a largely complete asymmetric unit of four chains (each pair of chains contains one-half of two crystallographically distinct four-helix bundles). Structural refinements were carried out using Refmac5 (*37*), XtalView (*43*), and ARP/wARP (*42*). The refined antiparallel model for peptide **2** was subsequently used as the initial model for molecular replacement (using Molrep) for the remaining antiparallel structures, with the exception of E20C L16G Y17H (peptide **10**). The structure of sequence **10** was determined with Phaser (*44*) using a truncated (residues 5−30) single strand from E20C L16G (peptide **9**) as a model for molecular replacement. The parallel crystal structures were determined using the GCN4-pLI (sequence **1**) structure as a model for molecular replacement with Molrep. The dataset for peptide **6** was collected on the same R-Axis IV as the other crystals but was aligned to a different emission edge (Cu Kβ, λ = 1.39 Å).

Root-mean-square deviation (rmsd) values were calculated using the Insight II group of software programs. Figures were generated using Pymol (*45*).

Molecular Dynamics. REX simulations were performed using the MMTSB Toolset (*46*) as an interface to the CHARMM simulation package (*47*). Unless otherwise noted, the simulated structures did not include residues 1 or 33, because these residues were typically not well-resolved in the crystal structures and were assumed to be unstructured and therefore not critical to the stability of either configuration. The N and C termini were capped with acetamide and *N*-methylamide groups, respectively. For each sequence, 10 replicas at temperatures exponentially distributed between 280 and 330 K were simulated, with exchanges attempted every 1 ps. The temperature range was chosen to be near room temperature, have an average temperature gap of 5 K, and have an upper temperature that would enhance side-chain sampling without approaching the simulated melting temperature (more below). The autocorrelation function of the parallel and antiparallel energies for the lowest temperature window indicates that each measurement is independent; that is, 1 ps is sufficient to permit relaxation at a new temperature after an exchange (data not shown). Acceptance ratios between neighboring windows were approximately 40%.

Each REX simulation was seeded with five parallel and five antiparallel structures (replicas). Starting structures for initial simulations consisted of five copies of the crystal structure and five structures of the opposite configuration, obtained by modeling the sequence into either the GCN4-

pLI (peptide **1**) or E20C (peptide **3**) crystal structures, as appropriate. Modeling tools provided by MMTSB were used for mutating sequences in silico. In several cases, duplicate simulations were initiated using structures resulting from the simulation of a different sequence (again, mutated with the tools provided by MMTSB) to provide an uncertainty estimate on the populations derived from the simulation. Each simulation was allowed to equilibrate for 200 ps, followed by at least 600 ps of production simulation, with some sequences extending up to 3 ns to better characterize convergence properties.

Each replica was simulated at the appropriate temperature with the molecular dynamics engine in CHARMM, using the velocity Verlet integrator and a 2-fs time step. The temperature of each replica was maintained with a Nosé−Hoover thermostat using a coupling constant of 50 kcal/s². The potential energy function consisted of the CHARMM22 all-atom force field (*48*) with ϕ/ψ dihedral cross terms (*49*) and the GBMV implementation (*50*) of the generalized Born equation as an implicit solvent model. Nonbonded interactions were not considered beyond 18 Å, with interactions in the last 2 Å being smoothly feathered to 0 with a cubic switching function. For the GB model, a dielectric of 80 was used for the bulk solvent; default Lennard−Jones R_{min}/2 radii and a 1.4 Å probe radius was used in the construction of the molecular volume. The Debye−Hückel screening length (κ) was set to 0, indicating a salt concentration of 0 M. Specific to the GBMV method, the grid-based angular integration scheme using concentric 38-point Lebedev spheres was chosen, and an empirical Coulomb field approximation (CFA) correction was employed with the default values (shift = −0.102, slope = −0.9085). While it is commonplace to augment a GB model with a coarse-grain model for nonpolar solvation of the form γ·SASA (where SASA is the solvent-accessible surface area in Å² and γ is a surface-tension coefficient usually taken to be 5 cal mol^{-1} Å^{-2}), no such term was applied here. Justification for this decision is 2-fold: we recently demonstrated that, for a series of small molecules, this nonpolar addition to the energy function impeded the ability of the solvation model to predict relative free energies of hydration (presumably because the impact of entropic loss from specific solvent ordering is to some degree offset by the absence of solute−solvent dispersion interactions in the model) (*51*), and in this particular application, the two configurations have very similar SASA, suggesting that the addition of such a term would not substantially favor either configuration.

Initial simulations indicated that the upper end of the temperature range permitted partial unfolding of some assemblies; the absence of solvent viscosity in implicit solvent models can accelerate such events. To limit the study to fully associated bundles, four flat-bottom, half-harmonic potentials were subsequently applied to restrain the cross-bundle helices (this pair is always parallel) from drifting apart. The C$_\alpha$'s of residue five of the cross-bundle pair and likewise for residue 30 were restrained with a 50 kcal mol^{-1} Å^{-2} harmonic potential if these distances separated by more than 14 Å. Unrestrained simulations that did not involve any partial unfolding at higher temperatures have been included to demonstrate that the inclusion of the restraints did not affect any results.

All reported populations are those found in the low-temperature window (280 K). In all cases, the simulations that produced the lowest average energy for each sequence also produced the lowest average energy for the dominant geometry (parallel or antiparallel) of all simulations for that sequence. It should be noted that, because of the short time scale simulated here, parallel and antiparallel configurations could not interchange during sampling. As a consequence, it is expected that a correct Boltzmann distribution cannot be obtained at all temperatures, and therefore, the populations reported should not be considered as predicted solution populations for that temperature. Instead, the REX methodology in this application should be treated merely as a conformational search tool for identifying low-energy configurations.

Standard errors of the mean for reported total and interaction energies range from 0.5 to 3.5 kcal/mol. Considering the slow convergence of populations, it is expected that this range may underestimate the true uncertainty.

Circular Dichroism (CD) Spectroscopy. Peptide stock solutions in buffer [5 mM 3-(*N*-morpholino)propanesulfonic acid (MOPS) at pH 7.0] were prepared at a concentration of 2 mg/mL and standardized by the measurement of tyrosine or ABA absorbance. Measurements were made in duplicate. The concentration was determined assuming $\epsilon_{274 \text{ nm}} = 1400$ M^{-1} cm^{-1} or 18069 M^{-1} cm^{-1} for tyrosine or ABA, respectively. Peptide stock solutions were stored at -80 °C and diluted to an appropriate concentration with buffer before use. Wavelength scans were recorded in 0.5 cm path-length cells at peptide concentrations of 20 μM in buffer (5 mM MOPS at pH 7.0), while thermal melts were measured for 10 μM peptide in buffer (50 mM phosphate, 150 mM NaCl at pH 7.0, and 4 M guanidine hydrochloride). Added dithiothreitol (0.5 mM) was included as the reducing agent for the peptides containing the E20C substitution. The temperature was increased in 2 °C intervals, with an equilibration time of 90 s before recording the CD signal at 222 nm. All thermal melts were reversible, with >90% helicity regained upon cooling the sample. The plot of molar ellipticity as a function of the temperature was fit as a fourth-order polynomial using Mathematica, and the melting temperature (T_m) was calculated as the point at which the second derivative of this function was 0.

Size-Exclusion Chromatography (SEC). Peptide stock solutions were prepared as described for CD experiments. SEC was performed at room temperature on a Superdex 75 10/30 column eluted with buffer (50 mM phosphate and 150 mM NaCl at pH 7.0) at a flow rate of 0.5 mL/min. Samples for calibration were bovine erythrocyte carbonic anhydrase [2 mg/mL; molecular weight (MW), 29 000], horse heart cytochrome *c* (1 mg/mL; MW, 12 384), bovine oxidized insulin B chain (2 mg/mL; MW, 3496), and cyanocobalamin (1 mg/mL; MW, 1355). Aliquots of each calibrant solution (20 μL) were mixed and injected. The elution volume was plotted against the MW and fit using a nonlinear regression with the program Mathematica. The peptide stock solutions were diluted with elution buffer to final concentrations of 250 μM, of which 50 μL was injected. Monitoring was carried out by ultraviolet (UV) absorption at 214 nm. Apparent aggregation (N_{agg}) states were calculated from the elution volume by first using the calibration plot to determine the apparent MW of the bundle and then dividing this value by the calculated MW of an individual peptide.

Equilibrium Disulfide-Exchange Assay. The helix configuration of E20S (peptide **4**) in solution was determined using a disulfide-exchange assay (*4*, *52*). Variants of the E20S sequence with an appended Cys-Gly-Gly sequence at the N terminus (E20S-Ncys, peptide **11**) or an appended Gly-Gly-Cys sequence at the C terminus (E20S-Ccys, peptide **12**) were synthesized. An additional N-terminal Tyr residue was also appended to peptide **12** to facilitate HPLC separation. These peptides (5 mg each) were mixed and air-oxidized for 12 h in 2:1 DMF/H$_2$O (5 mL) solution containing *N,N*-diisopropylethylamine (25 μL). The disulfide-bonded heterodimer (Ns-sC) and homodimers (Ns-sN and Cs-sC) were purified by HPLC; identities and purities were confirmed using MALDI—TOF and analytical HPLC, respectively. The exchange assay involved incubating either the heterodimer alone (Ns-sC) or an equimolar mixture of the homodimers (Ns-sN and Cs-sC) in redox buffer (30 μM total peptide, 50 mM HEPES at pH 8.0, 2.5 M guanidinium, 500 μM reduced glutathione, and 125 μM oxidized glutathione), allowing for the exchange of disulfide bonds. Guanidinium was required for the equilibration to proceed at reasonable rates; the molar ellipticity of peptide **4** in 2.5 M guanidinium is >95% of the ellipticity value measured in the absence of guanidinium. At desired times, an aliquot was removed and analyzed by HPLC.

RESULTS AND DISCUSSION

Peptide Variants. The following is the structural, computational, and biophysical analysis of a single peptide sequence observed to crystallize in both parallel and antiparallel tetrameric coiled-coil configurations. This sequence was discovered as follows.

In the course of a study directed at the design of peptide assemblies with aminoacyl transferase activity (*53*), crystals were obtained for peptide **2** (Table 1), which is derived from the parallel homotetrameric GCN4-pLI (sequence **1**) (*4*). Peptide **2** contains seven sites of substitution with respect to GCN4-pLI, none of which occur in hydrophobic core residues. Phases based on heavy atom soaking were used for the structural determination of **2**. To our surprise, **2** adopted an antiparallel crystallographic configuration (Figure S1 in the Supporting Information), an unexpected result given that **2** differed from GCN4-pLI (peptide **1**) only at solvent-exposed sites and exhibited interhelical aminoacyl-transfer activities consistent with a parallel assembly in solution. We proceeded in characterizing a set of backtracking amino acid substitutions to deduce the minimal set required to observe the antiparallel crystal structure (Table 1).

A variant of GCN4-pLI (sequence **1**) containing an N-terminal acetamidobenzoic acid (ABA) moiety (peptide **5**) crystallized in the same lattice and parallel configuration as **1**, indicating that ABA does not induce the structural change. Peptides **6** and **7**, which adopted the antiparallel crystallographic arrangements, likewise discounted the possibilities that four Lys → Arg amino acid substitutions or the Y17H substitution had caused the structural switch. We ultimately identified a single E20C amino acid substitution (peptide **3**) sufficient to alter the crystallographic configuration of GCN4-pLI from parallel to antiparallel. A variant of **3** in which C20 was alkylated with iodoacetamide, peptide **8**, also exhibited the antiparallel crystallographic structure,

Table 1: Sequences, PDB Entries, and Observed Crystallographic Topologies[a]

peptide	sequence	PDB ID	crystallographic configuration
1, GCN4-pLI[b]	Ac-RMKQIED-KLEEILS-KLYHIEN-ELARIKK-LLGER-OH	1GCL, 1UO2	parallel
2	**ABA**-RM**R**QIED-**R**LEEILS-KL**HH̄**I**C**N-ELARI**RR**-LLGER-OH	1W5K	antiparallel
3, E20C	Ac-RMKQIED-KLEEILS-KLYHI**C**N̄-ELARIKK-LLGER-OH	2CCN	antiparallel
4, E20S	Ac-RMKQIED-KLEEILS-KLYHI**S̄**N-ELARIKK-LLGER-OH	2CCF, 2CCE	antiparallel, parallel
5, ABA-pLI	**ABA**-RMKQIED-KLEEILS-KLYH̄IEN-ELARIKK-LLGER-OH	1W5I	parallel
6	**ABA**-RM**R**QIED-**R**LEEILS-KLYHI**C**N-ELARI**RR**-LLGER-OH	1W5J	antiparallel
7, E20C Y17H	**ABA**-RMKQIED-KLEEILS-KL**H**HI**C**N-ELARIKK-LLGER-OH	1W5H	antiparallel
8, E20C^Ak	Ac-RMKQIED-KLEEILS-KLYHI**C**^(A̅k̄)N-ELARIKK-LLGER-OH	1W5G	antiparallel
9, E20C L16G[b]	Ac-R-MKQIEDK-LEEILSK-**G**YHI**C**N̄E-LARIKKL-LGER-OH	1W5L	parallel
10, E20C L16G Y17H[b]	**ABA**-R-MKQIEDK-LEEILSK-**GH̄**HI**C**NE-LARIKKL-LGER-OH	2BNI	antiparallel
11	Ac-**CGG**RMKQIED-KLEEILS-KLYHI**S̄**N-ELARIKK-LLGER-OH		
12	Ac-**Y**RMKQIED-KLEEILS-KLYHI**S̄**N-ELARIKK-LLGER**GGC**-OH		

[a] Substitutions relative to GCN4-pLI are shown in bold, and position 20 is underlined. Ac, acetyl; ABA, acetamidobenzoic acid; C^Ak, cysteine alkylated with iodoacetamide. [b] The crystallization and structure determination of this peptide has been reported previously (*4, 17*).

indicating that the interaction between free sulfhydryl groups is not a determining factor in the formation of the antiparallel configuration. For a related study aimed at characterizing cavities in coiled-coil peptides (*17*), we prepared two peptides containing an L16G substitution (in the hydrophobic core) in addition to the E20C substitution (peptides **9** and **10**); while one of these peptides adopted the antiparallel configuration in the crystalline state (E20C L16G Y17H, peptide **10**), the other crystallized in the parallel configuration (E20C L16G, peptide **9**). Finally, we found that a peptide containing a single E20S substitution (peptide **4**) relative to GCN4-pLI crystallized (under different crystallization conditions) in both the parallel and antiparallel configurations; this was the only sequence observed to crystallize in both configurations.

Crystal Lattices. All sequences exhibiting the parallel configuration were crystallized from the same buffer condition and in the same crystal lattice. In the $P4_132$ space group of the parallel lattice, the four-helix bundle is generated by a crystallographic 2-fold symmetry axis acting on the two-stranded (parallel) asymmetric unit, so that 12 tetrameric bundles comprise the unit-cell contents. Because the parallel configuration of E20S (sequence **4**) crystallized in the same lattice as native GCN4-pLI (sequence **1**), their structures are very similar. All sequences adopting the antiparallel configuration crystallized in one of two symmetry-related lattices in space group $P4_22_12$ or $P2_12_12$ (unit-cell parameters were similar for both space groups), with the exception of the E20C L16G Y17H variant (peptide **10**), which was processed in the $P3_1$ space group. In the $P4_22_12$ space group of the E20S antiparallel crystal lattice, four-helix bundles are generated from a two-stranded (antiparallel) asymmetric unit; bundles stack with their major axis orthogonal to crystallographic 2-fold axes that generate the antiparallel four-helix bundle. Residues at surface positions form lattice contacts with adjacent, oppositely oriented chains.

Crystallographic Structures. The quaternary structure of both configurations can be described as a left-handed supercoil of α helices that forms a cylindrical assembly with a diameter of ~28 Å and a length of ~49 Å. Unlike the parallel E20S tetramer, which contains alternating "plates" of hydrophobic *a* residues (Leu) and *d* residues (Ile) (Figure 1a), the core of the antiparallel configuration comprises two sets of *a*–*a* and *d*–*d* hydrophobic "stripes" running along the bundle (Figure 1b). Backbone and core residue side-chain atoms of the two unique helices (residues 3–30) in the
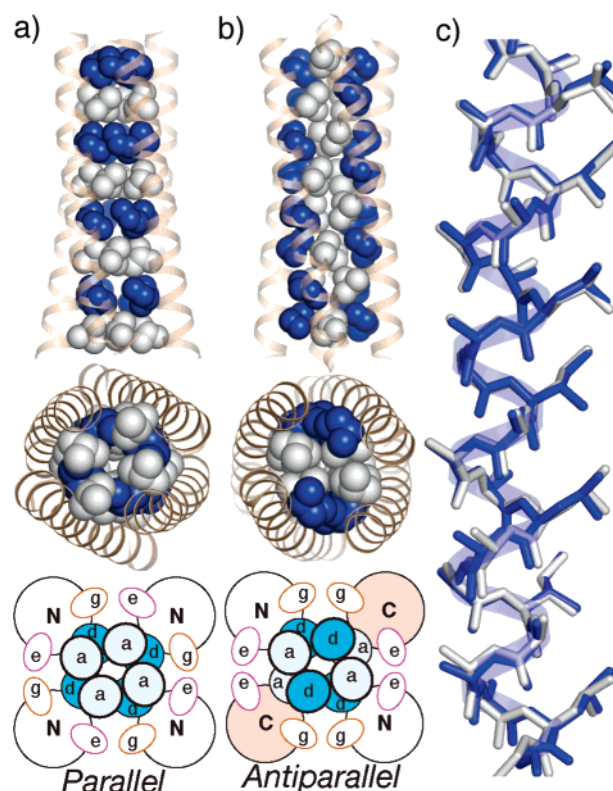

FIGURE 1: Crystal structures of the E20S variant (peptide **4**) in the parallel and antiparallel tetrameric configurations. Side and top views show the parallel (a) and antiparallel (b) structures, highlighting core Leu (white) and Ile (blue) residues, with schematic diagrams showing interhelical packing interactions. (c) Superposition of single helices from the antiparallel (blue) and parallel (beige) configurations. Backbone, β carbons, and core residue heavy atoms are shown.

parallel E20S configuration can be superimposed with a rmsd of 0.68 Å; a similar superposition of the two unique strands of the antiparallel structure yields a lower rmsd of 0.37 Å.

Crystallization of a single peptide sequence in two distinct structures indicates that the 2-folds must be relatively close in energy; comparing the two E20S configurations suggests a structural basis for this energetic similarity. First, individual helices from the two distinct structures exhibit highly analogous conformations, as indicated by a superposition of backbone and core residue side-chain atoms (Figure 1c). The average of the four rmsd values between unique helices from the different configurations is 0.53 Å, a lower value than
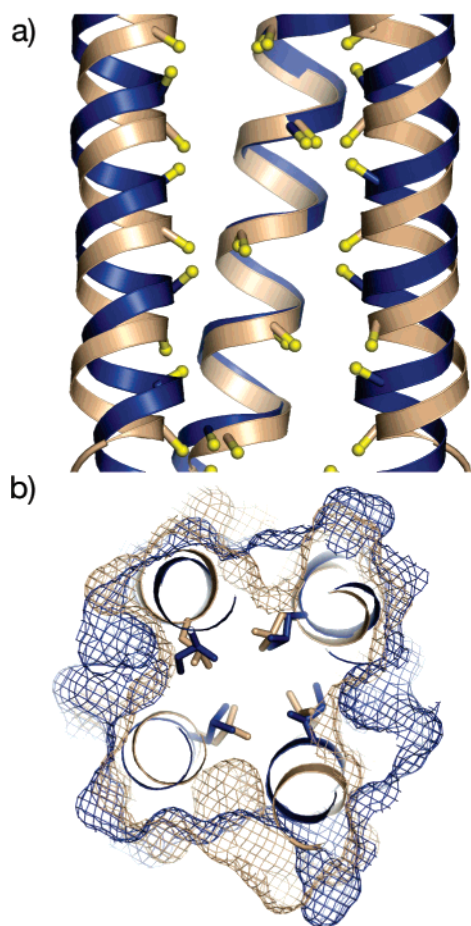
FIGURE 2: Comparison of hydrophobic packing interactions in the parallel and antiparallel E20S configurations. (a) Overlay of the antiparallel (blue) and parallel (beige) E20S structures shows the shifted register for two helices in the antiparallel tetramer (with one helix omitted for clarity). Cα−Cβ bonds of hydrophobic core residues are shown, with Cβ atoms colored yellow, to illustrate the altered core geometry imposed by the antiparallel configuration. (b) Cross-section of the same superposition showing the solvent-exposed surfaces of the antiparallel (blue mesh) and parallel (beige mesh) tetramers, along with side-chain atoms for hydrophobic core residues. While the surfaces of the two assemblies are dissimilar, the core residues closely overlap.

that of the two unique strands from the parallel structure (rmsd = 0.68 Å). Because helices from the two configurations are conformationally similar and are in equilibrium with an identical unfolded state, the difference in folding energetics for individual helices in these tetramers is necessarily small. Second, despite the different relative orientations of helices, the hydrophobic interaction surfaces of the parallel and antiparallel tetramers are strikingly similar. Diagonal helices in the antiparallel configuration shift register by ∼1 Å relative to equivalent chains in the parallel assembly (Figure 2a), apparently to allow for knob-in-hole core packing by counteracting the altered Cα−Cβ vectors that result from changing the N → C sense of the strand. A cross-sectional view of the superposed tetramers indicates that, whereas the solvent-exposed surfaces of the assemblies vary considerably, the hydrophobic core surfaces closely align (Figure 2b). Third, subtle conformational changes to polar residues on the solvent-exposed faces allow for the formation of favorable electrostatic contacts and avoidance of unfavorable contacts in both the parallel and antiparallel configurations. In GCN4-pLI (peptide **1**), a salt bridge is observed

between Lys15 and Glu20 (Figure 3a). This contact obviously cannot form in the parallel configuration of E20S (sequence **4**) but is replaced by polar interactions between Lys15, Ser20, His18, and bridging water molecules that leave the overall pattern of polar contacts between helices largely unchanged (parts a and b of Figure 3). The antiparallel configuration of E20S places Lys15 residues near each other on the g−g′ faces, but this seemingly unfavorable electrostatic situation (assuming both Lys residues are protonated) is largely negated by the flexibility of the Lys15 side chains, which allows for the terminal ammonium groups to project away from each other and form charge-pair contacts with other residues (Figure 3c). Such behavior indicates that interhelical electrostatic interactions in coiled-coil assemblies can be context-dependent. Ser20 residues from adjacent helices are directed toward each other at the center of the antiparallel E20S bundle and form a polar contact mediated by a water molecule (Figure 3d). In short, the hydrophobic and electrostatic patterning of these GCN4-derived coiled coils is such that both parallel and antiparallel configurations can be accommodated with just minor changes to the helix register and side-chain conformations.

REX Simulations. To gain a deeper understanding of the delicate energetic balance between the parallel and antiparallel configurations, we initiated molecular dynamics simulations. A known deficiency of such simulations using modern classical force fields is the limited time scale accessible with finite computing resources. Even with enhanced sampling techniques, such as umbrella sampling, the ability to characterize the conformational energetics of two rearranged topologies, such as the parallel to antiparallel geometries described here, is difficult at best. Instead, we utilized the well-documented REX methodology (*35*) to permit a thermodynamic "competition" between parallel and antiparallel assemblies. See the Materials and Methods for a brief discussion on why these populations should not be considered predictions on relative populations at 280 K; instead, the intention of the simulations was to identify sequences for which there is significant enrichment in antiparallel structures that are competitive in energy with parallel configurations.

The percentage of parallel structures found in the lowest temperature window of the REX simulations is reported in Table 2 (percentage of antiparallel = 1 − % parallel, because unfolded, partially unfolded, and alternative topologies were not sampled). Duplicate simulations of a given sequence reveal that in many cases the convergence of the populations is slow. For example, the percentage of parallel for E20C (peptide **3**) ranges from 28 to 64%. Despite the variability, a consistent trend is clear. All simulations with Glu at position 20 were dominated by parallel structures (88−100%), whereas all simulations with Cys or Ser at position 20 exhibit a substantial enrichment in antiparallel structures [percentage of parallel dropping to 17−64% in all simulations but one, where a high energy simulation of E20C Y17H (peptide **7**) stayed 95% parallel even after 3 ns]. If one treats the simulations that produced the lowest average energy structures for each sequence as the most reliable, a considerably tighter range for the percentage of parallel emerges for all sequences with an E20 substitution (17−32%). Finally, it should be noted that the use of restraints to maintain the overall topology at higher temperature windows had no apparent effect on the calculated energies.
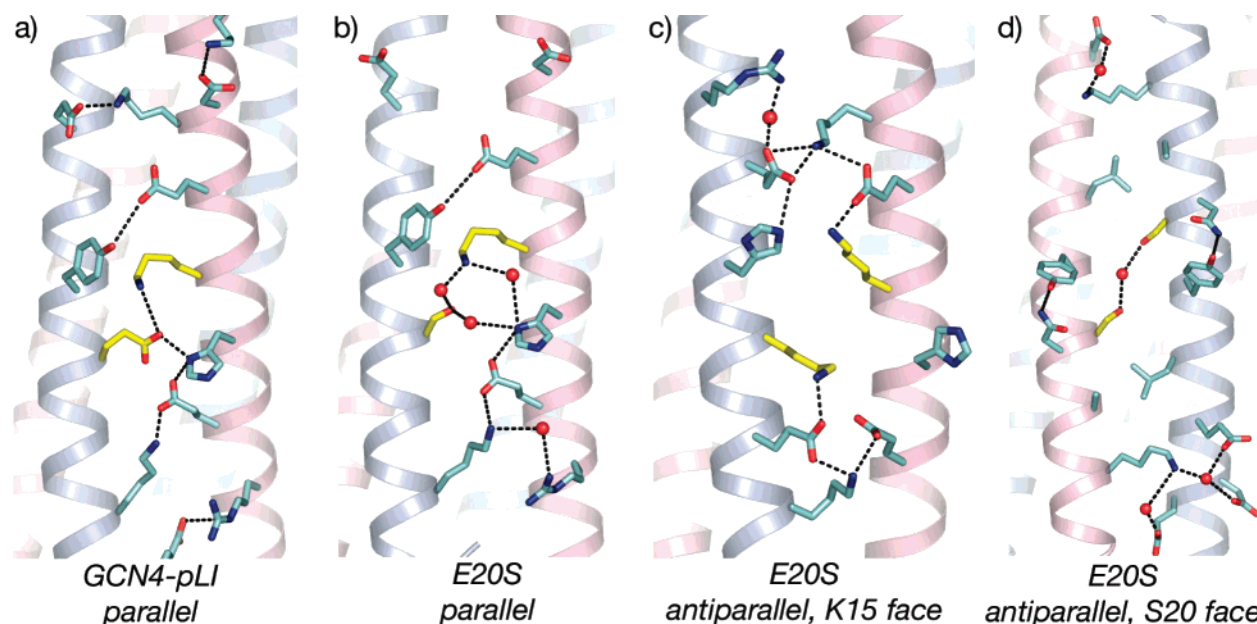
FIGURE 3: Electrostatic interaction surfaces for the parallel and antiparallel coiled-coil tetramers. Dotted black lines are shown for potential polar intra- and interhelical interactions (<4 Å) between surface residues for (a) GCN4-pLI, (b) E20S in the parallel configuration, (c) E20S in the antiparallel configuration (K15 face), and (d) E20S in the antiparallel configuration (S20 face). Positions 15 and 20 are colored yellow. Bridging water molecules are shown as red spheres.

Table 2: Summary of Populations in the Lowest Temperature (280 K) Window of 10-Window REX Simulations[a]

| | percentage of parallel | | |
peptide	with restraints	no restraints	crystallographic configuration
1, GCN4-pLI	89 (1.0 ns), 98 (1.0 ns), *100* (1.0 ns), 88 (0.8 ns)	**96** (2.8 ns)	parallel
1, GCN4-pLI (1−33)[b]	**88** (0.8 ns)	ND	parallel
L9A GCN4-pLI[c]	ND	**94** (2.8 ns)	parallel
L23G GCN4-pLI[c]	ND	**95** (1.8 ns)	parallel
I26G GCN4-pLI[c]	**99** (1.0 ns)	ND	parallel
3, E20C	64 (1.7 ns), 31 (1.5 ns), **32** (1.5 ns), *28* (0.9 ns)	32 (3.0 ns)	antiparallel
3, E20C (1−33)[b]	28 (0.8 ns)	ND	antiparallel
4, E20S	71 (1.3 ns), **24** (1.3 ns), 44 (1.2 ns)	ND	parallel, antiparallel
7, E20C Y17H	**26** (1.6 ns)	95 (3.0 ns)	antiparallel
9, E20C L16G	54 (1.1 ns), **27** (1.0 ns), 54 (0.6 ns)	49 (2.8 ns)	parallel
10, E20C Y17H L16G	ND	**17** (2.8 ns)	antiparallel

[a] If multiple simulations were performed starting from different initial conditions for a given sequence, they are all listed along with the duration of the simulation. The simulation resulting in the lowest average energy for a particular sequence is denoted in bold. Italics indicate that the simulation was run with the new rotational invariant version of the GBMV algorithm (63). [b] The full-length sequence (residues 1−33), rather than a truncated sequence (residues 2−32), was used for simulation. [c] This variant of GCN4-pLI, containing an amino acid substitution in the hydrophobic core, has previously been shown to crystallize in the parallel configuration (17).

Table 3: Decomposition of Total Potential Energies (in kcal/mol) from the Lowest Temperature Window (280 K) of Lowest Average Energy Simulations of GCN4-pLI (**1**) and E20C (**3**)

| | GCN4-pLI (**1**) | | E20C (**3**) | |
	parallel	antiparallel	parallel	antiparallel
Lennard−Jones + bonded	1591.4	1622.7	1570.4	1596.8
electrostatics + GB	−5676.7	−5686.3	−5317.4	−5362.3

The dominant interactions from representative lowest energy simulations of the parallel GCN4-pLI (peptide **1**) and the antiparallel E20C (peptide **3**) are shown in Table 3. This potential energy breakdown reveals that, for both sequences, electrostatic interactions favor the antiparallel geometry, while packing interactions (Lennard−Jones plus bonded terms) favor the parallel configuration. The presence of Glu20 dramatically minimizes the electrostatic preference for the antiparallel configuration, thereby allowing for the packing interactions to dominate the overall folding energetics and therefore favor the parallel configuration. On the other

hand, substituting Glu20 leads to an energetic clash between the opposing electrostatic and packing preferences, such that the overall free energy of the two configurations is apparently close enough to produce the structural heterogeneity reported here. One implication of the electrostatic preference for antiparallel configurations is that electrostatic screening from high ionic concentrations should favor parallel structures, as may be the case in the crystallization buffer yielding parallel assemblies (containing 2.0 M NaCl) or in the buffer of the disulfide-exchange assay described below (containing 2.5 M guanidinium).

Glu20 preferentially stabilizes the parallel configuration via electrostatic interactions, as evidenced by comparing the simulated interaction energies between Glu20 and the rest of the tetramer (Table 4). This preference for the parallel geometry likely stems from the interhelical salt bridge between Glu20 and Lys15 in the parallel geometry; Glu20 only makes intrahelical contacts in the simulated antiparallel

Table 4: Average Interaction Energies (in kcal/mol) for Residue 20 of GCN4-pLI (**1**, Residue 20 = Glu) and E20C (**3**) with the Entire System Including and Excluding Interaction Energies for Lys15[a]

	GCN4-pLI (**1**)		E20C (**3**)	
	parallel	antiparallel	parallel	antiparallel
	Including Lys15			
Lennard−Jones	−28.5	−36.0	−44.2	−51.4
electrostatics + GB	−476.4	−419.3	−59.7	−60.0
	Excluding Lys15			
Lennard−Jones	−36.4	−35.4	−41.2	−50.4
electrostatics + GB	1018.4	1078.4	689.2	689.2

[a] Data taken from the lowest temperature window (280 K) of lowest-energy simulations.

Table 5: Apparent Aggregation States, Molar Ellipticals, and Thermal Denaturation Values for Selected Peptides

peptide	N_{agg}[a]	$[\theta]_{222}$[b]	T_m (°C)[c]
1, GCN4-pLI	3.8	−30 000	68
3, E20C	3.9	−29 600	80
4, E20S	4.1	−30 900	79
8, E20C^{Ak}	4.3	−28 400	83
9, E20C L16G	3.9	−27 400	37[d]
10, E20C L16G Y17H	3.7[e]	−27 000	37[d]

[a] Apparent aggregation number as measured by SEC. Estimated errors are ±0.1. [b] Molar ellipticity values (reported in deg cm² dmol⁻¹) at 222 nm for 20 μM peptide solutions in buffer (5 mM MOPS at pH 7.0). For sequences containing a free Cys residue, 0.5 mM dithiothreitol was included as a reducing agent. [c] Thermal denaturation as determined by CD for 10 μM peptide solutions in buffer (50 mM phosphate at pH 7.0 and 150 mM NaCl) containing 4 M guanidinium hydrochloride. For sequences containing a free Cys residue, 0.5 mM dithiothreitol was included as a reducing agent. [d] Performed with 1 M guanidinium hydrochloride. [e] Approximately 20% of the sample eluted with an N_{agg} of 3.0.

conformation. However, stabilization of the parallel configuration is not confined to the interaction with Lys15. In fact, the electrostatic interaction energy between Glu20 and the rest of the tetramer not including Lys15 favors the parallel structure as well (Table 4), suggesting more favorable solvation or a long-range stabilization of the charge on Glu20 in the parallel assembly or a destabilizing repulsion involving Glu20 residues in the antiparallel configuration. The difference in Lennard−Jones interaction energies for Glu20 and the rest of the system is apparently a function of the electronic repulsion that accompanies the strong electrostatic pairing with Lys15; that is, the difference in parallel/antiparallel Lennard−Jones interaction energies is significant when Lys15 is included but disappears when Lys15 is removed from the interaction calculation (Table 4). However, the interaction energies for Cys20 reveal differences in the Lennard−Jones interaction energies despite comparable electrostatics. While the latter observation suggests that the enrichment of antiparallel structures in REX simulations for sequences with the E20C substitution results in part from improved Cys packing in the antiparallel configuration, alkylation of the Cys (peptide **8**) did not preclude the antiparallel configuration.

Solution Characterization. To complement the crystallographic and computational analysis of the closely related sequences described above, we determined solution characteristics for a subset of peptides. Measured molar ellipticity values indicated very little difference in the helical content for the substituted peptides relative to GCN4-pLI (peptide **1**); even the sequences containing the L16G substitution in the hydrophobic core (peptides **9** and **10**) retain ≥90% helicity (Table 5 and Figure S2 in the Supporting Information). SEC indicated that all of the examined peptides were tetrameric in solution, although approximately 20% of the sample for E20C L16G Y17H (sequence **10**) eluted with a trimeric aggregation state (Table 5). Thermal denaturation studies (as determined by CD) indicated that the presence of Glu20 destabilizes the overall coiled-coil assembly by 11−15 °C relative to peptides with a substitution at this site (Table 5 and Figure S3 in the Supporting Information). This stability difference was somewhat surprising because Glu20 residues form interhelical salt bridges with Lys15 residues in the GCN4-pLI crystal structure, but this finding is nonetheless consistent with a previous study indicating that Glu20 is energetically destabilizing in the closely related parallel dimeric coiled-coil GCN4-p1 (*54*). Considering that Glu20 preferentially stabilizes the parallel configuration (described above), we suggest that Glu20 in these peptides

and the native GCN4 protein may help guide the formation of parallel helical assemblies at the expense of energetic stability. Single residues in the hydrophobic core (*52*) or on the surface (*55*, *56*) have similarly been implicated in encouraging structural uniqueness in other coiled-coil contexts. Although possible, results from an equilibrium disulfide-exchange assay (described below) make it unlikely that the higher T_m values result from significantly increased populations of antiparallel assemblies in solution.

To determine the helical configuration of E20S in solution, we carried out an equilibrium disulfide-exchange assay, which uses the relative populations of disulfide-bonded parallel and antiparallel dimers at equilibrium to reveal thermodynamically preferred strand orientations (Figure 4a) (*4*, *52*). Derivatives of E20S (**4**) were prepared by appending a Cys residue to either the N or C terminus via a flexible Gly-Gly linker (peptides **11** and **12**, respectively), and disulfide-bonded dimers of these sequences were allowed to equilibrate under redox conditions. The experiment supports the formation of predominantly parallel coiled coils in solution for E20S, because the antiparallel disulfide-bonded dimer rearranges to form only the parallel dimers at equilibrium (Figure 4b). While the antiparallel configuration must be present in at least low concentrations (because it crystallizes), we also note that, considering the requisite similarity in energy between the two configurations, the differences in buffer conditions between the crystallization and disulfide-exchange experiments may influence the relative population of parallel and antiparallel assemblies.

Implications. The clear implication of the experiments detailed here is that many coiled-coil sequences may be delicately poised to adopt various quaternary structures that are similar in overall energy. The coiled coil is not only built from monomers comprised of a relatively simple pattern of hydrophobic and polar residues but also is usually an assembly of identical, noncovalently associated subunits; these properties lend themselves to the formation of multiple oligomerization states and configurations. Together with the previous examples of structural nonspecificity in GCN4-derived peptides, the observation of parallel and antiparallel crystallographic configurations from a single sequence not only emphasizes the predisposition of the coiled-coil motif to adopt multiple conformations but also calls attention to
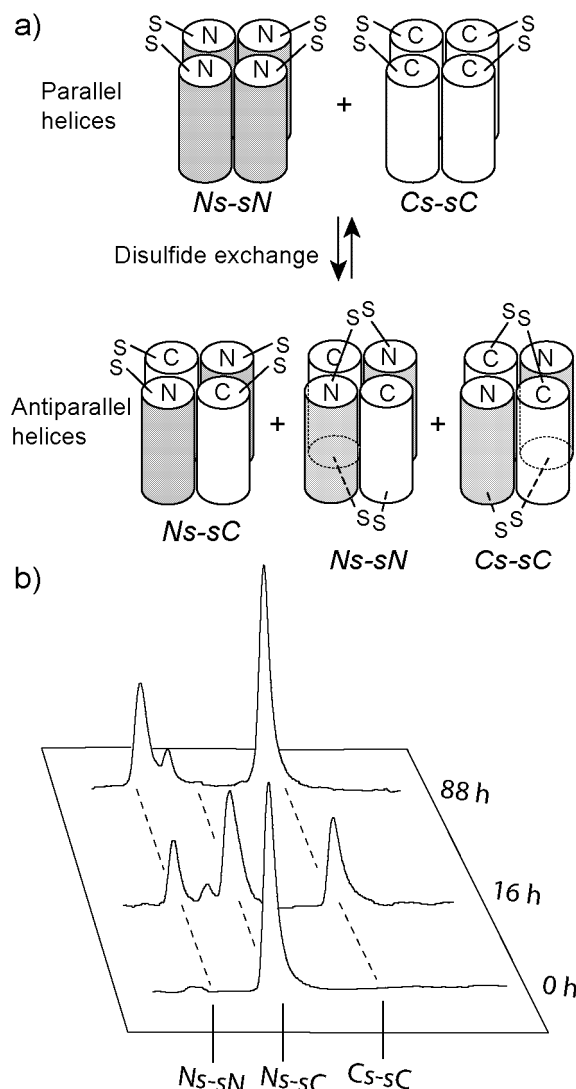
FIGURE 4: Equilibrium disulfide-exchange assay for E20S (**4**). (a) Assuming the glycyl linkers allow random sorting of the terminal thiols, tetramers in the parallel configuration will form only parallel homodimeric disulfides, whereas antiparallel tetramers will also form the antiparallel heterodimeric disulfide. (b) HPLC traces showing disulfide exchange over the course of the equilibration. The disulfide-bonded antiparallel heterodimer (Ns-sC, 30 μM) rearranges to form only the parallel homodimers (Ns-sN and Cs-sC). In an analogous experiment initiated with equimolar amounts of the parallel dimers, no change was observed after 88 h, indicating that the system is at equilibrium. Peptide **12** has a larger extinction coefficient than peptide **11** because it contains an added tyrosine residue to facilitate HPLC separation. The small peak eluting between Ns-sN and Ns-sC is a disulfide adduct of glutathione to peptide **11**.

the associated risk that assumed (or even observed) structures may not represent the major species present in solution.

Viewed in this context, we propose that several recent reports of unexpected structural phenomena in coiled-coil proteins may in fact result from the presence of multiple topologies in solution (*57*). As an example, an A31P mutant of the ROP protein was recently shown to crystallize in a right-handed, mixed parallel/antiparallel four-helix bundle topology (*58*, *59*), as opposed to the left-handed all-antiparallel configuration of the native sequence (*60*). The protein unexpectedly retained partial biological activity (RNA binding) despite the drastic structural change, leading the authors to tentatively suggest that the binding might be restored in the mutant by a helix rotation of ~35°, followed by a register shift of 4.8 Å relative to the crystallized structure (*58*). We suggest an alternative explanation: that the sequence populates both the crystallized structure (which is unlikely to bind RNA), as well as another fold more similar to the native structure, and thus competent to bind RNA. Another recent case involves the coiled-coil protein phospholamban, for which a water-soluble derivative is known to form a mixture of tetramers and pentamers in solution (*61*). The sequence was crystallized as an antiparallel tetramer (*62*), an unexpected finding given that the hydrophobic core residues are identical to those in GCN4-pLI (a parallel tetramer) and because the configuration of the native protein is a parallel pentamer. While it is possible that the assemblies in solution switch between the antiparallel tetramer and the parallel pentamer, as the authors suggest, another possibility is that parallel tetramers are also present and act as intermediates in the topological conversion.

The finding that a single solvent-exposed amino acid substitution can alter the observed structure of a coiled-coil tetramer illustrates the sensitivity of the structure to sequence, underscores the complexity of interactions inherent in even simple macromolecules, and will hopefully raise awareness of the potentially significant structural ramifications of seemingly innocuous amino acid substitutions in coiled-coil assemblies. Further, the structures reported here may facilitate the structure-based design of antiparallel helical proteins.

NOTE ADDED IN PROOF

Subsequent to the acceptance of this manuscript, a structural characterization of antiparallel tetrameric coiled coils has appeared in which three charged amino acids at g heptad positions were substituted with hydrophobic residues. See: Deng, Y., Liu, J., Zheng, Q., Kallenbach, N. R., Lu, M. (2006) Antiparallel four-stranded coiled coil specified by a 3-3-1 hydrophobic heptad repeat, *Structure 14*, 247−255.

SUPPORTING INFORMATION AVAILABLE

Additional figures, CD wavelength scans, thermal denaturation curves, crystallization statistics. This material is available free of charge via the Internet at http://pubs.acs.org.

REFERENCES

1. Crick, F. H. C. (1953) The packing of α-helices: Simple coiled-coils, *Acta Crystallogr. 6*, 689−697.
2. Alber, T. (1993) How GCN4 binds DNA, *Curr. Biol. 3*, 182−184.
3. O'Shea, E. K., Klemm, J. D., Kim, P. S., and Alber, T. (1991) X-ray structure of the GCN4 leucine zipper, a two-stranded, parallel coiled coil, *Science 254*, 539−544.
4. Harbury, P. B., Zhang, T., Kim, P. S., and Alber, T. (1993) A switch between two-, three-, and four-stranded coiled coils in GCN4 leucine zipper mutants, *Science 262*, 1401−1407.
5. Harbury, P. B., Kim, P. S., and Alber, T. (1994) Crystal structure of an isoleucine-zipper trimer, *Nature 371*, 80−83.

6. Gonzalez, L., Jr., Woolfson, D. N., and Alber, T. (1996) Buried polar residues and structural specificity in the GCN4 leucine zipper, *Nat. Struct. Biol. 3*, 1011−1018.

7. Gonzalez, L., Jr., Brown, R. A., Richardson, D., and Alber, T. (1996) Crystal structures of a single coiled-coil peptide in two oligomeric states reveal the basis for structural polymorphism, *Nat. Struct. Biol. 3*, 1002−1010.

8. Gonzalez, L., Jr., Plecs, J. J., and Alber, T. (1996) An engineered allosteric switch in leucine-zipper oligomerization, *Nat. Struct. Biol. 3*, 510−515.

9. Eckert, D. M., Malashkevich, V. N., and Kim, P. S. (1998) Crystal structure of GCN4-pIQI, a trimeric coiled coil with buried polar residues, *J. Mol. Biol. 284*, 859−865.

10. Lu, M., Shu, W., Ji, H., Spek, E., Wang, L., and Kallenbach, N. R. (1999) Helix capping in the GCN4 leucine zipper, *J. Mol. Biol. 288*, 743−752.

11. Shu, W., Ji, H., and Lu, M. (1999) Trimerization specificity in HIV-1 gp41: Analysis with a GCN4 leucine zipper model, *Biochemistry 38*, 5378−5385.

12. Mittl, P. R. E., Deillon, C., Sargent, D., Liu, N., Klauser, S., Thomas, R. M., Gutte, B., and Grutter, M. G. (2000) The retro-GCN4 leucine zipper sequence forms a stable three-dimensional structure, *Proc. Natl. Acad. Sci. U.S.A. 97*, 2562−2566.

13. Akey, D. L., Malashkevich, V. N., and Kim, P. S. (2001) Buried polar residues in coiled-coil interfaces, *Biochemistry 40*, 6352−6360.

14. Lee, D. L., Ivaninskii, S., Burkhard, P., and Hodges, R. S. (2003) Unique stabilizing interactions identified in the two-stranded α-helical coiled-coil: Crystal structure of a cortexillin I/GCN4 hybrid coiled-coil peptide, *Protein Sci. 12*, 1395−1405.

15. Holton, J., and Alber, T. (2004) Automated protein crystal structure determination using ELVES, *Proc. Natl. Acad. Sci. U.S.A. 101*, 1537−1542.

16. Horne, W. S., Yadav, M. K., Stout, C. D., and Ghadiri, M. R. (2004) Heterocyclic peptide backbone modifications in an α-helical coiled coil, *J. Am. Chem. Soc. 126*, 15366−15367.

17. Yadav, M. K., Redman, J. E., Leman, L. J., Alvarez-Gutierrez, J. M., Zhang, Y., Stout, C. D., and Ghadiri, M. R. (2005) Structure-based engineering of internal cavities in coiled-coil peptides, *Biochemistry 44*, 9723−9732.

18. Kohn, W. D., and Hodges, R. S. (1998) De novo design of α-helical coiled coils and bundles: Models for the development of protein design principles, *Trends Biotechnol. 16*, 379−389.

19. Micklatcher, C., and Chmielewski, J. (1999) Helical peptide and protein design, *Curr. Opin. Chem. Biol. 3*, 724−729.

20. Oakley, M. G., and Hollenbeck, J. J. (2001) The design of antiparallel coiled coils, *Curr. Opin. Struct. Biol. 11*, 450−457.

21. Gernert, K. M., Surles, M. C., Labean, T. H., Richardson, J. S., and Richardson, D. C. (1995) The Alacoil: A very tight, antiparallel coiled-coil of helixes, *Protein Sci. 4*, 2252−2260.

22. Betz, S. F., and DeGrado, W. F. (1996) Controlling topology and native-like behavior of de novo-designed peptides: Design and characterization of antiparallel four-stranded coiled coils, *Biochemistry 35*, 6955−6962.

23. Monera, O. D., Zhou, N. E., Lavigne, P., Kay, C. M., and Hodges, R. S. (1996) Formation of parallel and antiparallel coiled-coils controlled by the relative positions of alanine residues in the hydrophobic core, *J. Biol. Chem. 271*, 3995−4001.

24. McClain, D. L., Woods, H. L., and Oakley, M. G. (2001) Design and characterization of a heterodimeric coiled coil that forms exclusively with an antiparallel relative helix orientation, *J. Am. Chem. Soc. 123*, 3151−3152.

25. Gurnon, D. G., Whitaker, J. A., and Oakley, M. G. (2003) Design and characterization of a homodimeric antiparallel coiled coil, *J. Am. Chem. Soc. 125*, 7518−7519.

26. Schnarr, N. A., and Kennan, A. J. (2004) Strand orientation by steric matching: A designed antiparallel coiled-coil trimer, *J. Am. Chem. Soc. 126*, 14447−14451.

27. Hill, R. B., and DeGrado, W. F. (1998) Solution structure of a2D, a native-like de novo designed protein, *J. Am. Chem. Soc. 120*, 1138−1145.

28. Lovejoy, B., Choe, S., Cascio, D., McRorie, D. K., DeGrado, W. F., and Eisenberg, D. (1993) Crystal structure of a synthetic triple-stranded α-helical bundle, *Science 259*, 1288−1293.

29. Schafmeister, C. E., LaPorte, S. L., Miercke, L. J. W., and Stroud, R. M. (1997) A designed four helix bundle protein with native-like structure, *Nat. Struct. Biol. 4*, 1039−1046.

30. Schafmeister, C. E., Miercke, L. J. W., and Stroud, R. M. (1993) Structure at 2.5 Å of a designed peptide that maintains solubility of membrane proteins, *Science 262*, 734−738.

31. Burkhard, P., Strelkov, S. V., and Stetefeld, J. (2001) Coiled coils: A highly versatile protein folding motif, *Trends Cell Biol. 11*, 82−88.

32. Lupas, A. (1996) Coiled coils: New structures and new functions, *Trends Biochem. Sci. 21*, 375−382.

33. Rose, A., and Meier, I. (2004) Scaffolds, levers, rods and springs: Diverse cellular functions of long coiled-coil proteins, *Cell. Mol. Life Sci. 61*, 1996−2009.

34. Weninger, K., Bowen, M. E., Chu, S., and Brunger, A. T. (2003) Single-molecule studies of SNARE complex assembly reveal parallel and antiparallel configurations, *Proc. Natl. Acad. Sci. U.S.A. 100*, 14800−14805.

35. Nymeyer, H., Gnanakaran, S., and Garcia, A. E. (2004) Atomic simulations of protein folding, using the replica exchange algorithm. *Methods Enzymol. 383*, 119−149.

36. Pflugrath, J. W. (1999) The finer things in X-ray diffraction data collection, *Acta Crystallogr., Sect. D: Biol. Crystallogr. 55*, 1718−1725.

37. The CCP4 suite: Programs for protein crystallography. (1994) *Acta Crystallogr., Sect. D: Biol. Crystallogr. 50*, 760−763.

38. Potterton, E., Briggs, P., Turkenburg, M., and Dodson, E. (2003) A graphical user interface to the CCP4 program suite, *Acta Crystallogr., Sect. D: Biol. Crystallogr. 59*, 1131−1137.

39. Terwilliger, T. C. (2003) Automated main-chain model building by template matching and iterative fragment extension, *Acta Crystallogr., Sect. D: Biol. Crystallogr. 59*, 38−44.

40. Terwilliger, T. C. (2000) Maximum-likelihood density modification, *Acta Crystallogr., Sect. D: Biol. Crystallogr. 56*, 965−972.

41. Terwilliger, T. C., and Berendzen, J. (1999) Automated MAD and MIR structure solution, *Acta Crystallogr., Sect. D: Biol. Crystallogr. 55*, 849−861.

42. Perrakis, A., Harkiolaki, M., Wilson, K. S., and Lamzin, V. S. (2001) ARP/wARP and molecular replacement, *Acta Crystallogr., Sect. D: Biol. Crystallogr. 57*, 1445−1450.

43. McRee, D. E. (1999) XtalView/Xfit—A versatile program for manipulating atomic coordinates and electron density, *J. Struct. Biol. 125*, 156−165.

44. Storoni, L. C., McCoy, A. J., and Read, R. J. (2004) Likelihood-enhanced fast rotation functions, *Acta Crystallogr., Sect. D: Biol. Crystallogr. 60*, 432−438.

45. DeLano, W. L. The PyMOL Molecular Graphics System; http://www.pymol.org.

46. Feig, M., Karanicolas, J., and Brooks, C. L., III (2004) MMTSB tool set: Enhanced sampling and multiscale modeling methods for applications in structural biology, *J. Mol. Graphics Modell. 22*, 377−395.

47. Brooks, B. R., Bruccoleri, R. E., Olafson, B. D., States, D. J., Swaminathan, S., and Karplus, M. (1983) CHARMM: A program for macromolecular energy, minimization, and dynamics calculations, *J. Comput. Chem. 4*, 187−217.

48. MacKerell, A. D. J., Bashford, D., Bellott, M., Dunbrack, R. L., Jr., Evanseck, J. D., Field, M. J., Fischer, S., Gao, J., Guo, H., Ha, S., Joseph-McCarthy, D., Kuchnir, L., Kuczera, K., Lau, F. T. K., Mattos, C., Michnick, S., Ngo, T., Nguyen, D. T., Prodhom, B., Reiher, W. E. I., Roux, B., Schlenkrich, M., Smith, J. C., Stote, R., Straub, J., Watanabe, M., Wiorkiewicz-Kuczera, J., Yin, D., and Karplus, M. (1998) All-atom empirical potential for molecular modeling and dynamics studies of proteins, *J. Phys. Chem. B 102*, 3586−3616.

49. MacKerell, A. D. J., Feig, M., and Brooks, C. L., III (2004) Improved treatment of the protein backbone in empirical force fields, *J. Am. Chem. Soc. 126*, 698−699.

50. Lee, M. S., Salsbury, F. R., and Brooks, C. L., III (2002) Novel generalized Born methods, *J. Chem. Phys. 116*, 10606−10614.

51. Price, D. J., and Brooks, C. L., III (2005) Detailed considerations for a balanced and broadly applicable force field: A study of substituted benzenes modeled with OPLS-AA, *J. Comput. Chem. 26*, 1529−1541.

52. Lumb, K. J., and Kim, P. S. (1995) A buried polar interaction imparts structural uniqueness in a designed heterodimeric coiled coil, *Biochemistry 34*, 8642−8648.

53. Wilcoxen, K. M. (2002) Ph.D. Thesis, The Scripps Research Institute, La Jolla, CA.

54. Lumb, K. J., and Kim, P. S. (1995) Measurement of interhelical electrostatic interactions in the GCN4 leucine zipper, *Science 268*, 436−439.

55. Hill, R. B., and DeGrado, W. F. (2000) A polar, solvent-exposed residue can be essential for native protein structure, *Structure 8*, 471−479.

56. Hill, R. B., Hong, J.-K., and DeGrado, W. F. (2000) Hydrogen bonded cluster can specify the native state of a protein, *J. Am. Chem. Soc. 122*, 746−747.

57. Levy, Y., Cho, S. S., Shen, T., Onuchic, J. N., and Wolynes, P. G. (2005) Symmetry and frustration in protein energy landscapes: A near degeneracy resolves the Rop dimer-folding mystery, *Proc. Natl. Acad. Sci. U.S.A. 102*, 2373−2378.

58. Glykos, N. M., Cesareni, G., and Kokkinidis, M. (1999) Protein plasticity to the extreme: Changing the topology of a 4-α-helical bundle with a single amino acid substitution, *Structure 7*, 597−603.

59. Glykos, N. M., and Kokkindis, M. (2004) Structural polymorphism of a marginally stable 4-α-helical bundle, *Proteins: Struct., Funct., Bioinf. 56*, 420−425.

60. Banner, D. W., Kokkinidis, M., and Tsernoglou, D. (1987) Structure of the ColE1 Rop protein at 1.7 Å resolution, *J. Mol. Biol. 196*, 657−675.

61. Slovic, A. M., Summa, C. M., Lear, J. D., and DeGrado, W. F. (2003) Computational design of a water-soluble analog of phospholamban, *Protein Sci. 12*, 337−348.

62. Slovic, A. M., Stayrook, S. E., North, B., and DeGrado, W. F. (2005) X-ray structure of a water-soluble analog of the membrane protein phospholamban: Sequence determinants defining the topology of tetrameric and pentameric coiled coils, *J. Mol. Biol. 348*, 777−787.

63. Im, W., Chen, J., Price, D. J., and Brooks, C. L., III (2005) Manuscript in preparation.